Article | Open Access

Energy Materials

Sun *et al. Energy Mater.* **2026**, *6*, 600165 **DOI:**10.20517/energymater.2026.309

# Graphdiyne-enabled interfacial transport sieving for efficient and sustainable carbon-based perovskite photovoltaics

**Haochun Sun[1,2,#], Wenqiang Fan[1,2,#], Chenzhe Xu[1,2,#], Yingcong Liu[1,2], Hongwei Wang[1,2], Liyan Hu[1,2], Zhuojian Liang[1,2,*], Linkai Yu[1,2], Yijian Lu[1,2], Zhuo Kang[1,2,*], Yue Zhang[1,2,*]**

**Keywords:**
Carbon electrode-based perovskite solar cells, graphdiyne, interfacial transport sieving, hole extraction, lead sequestration

**Citation:** Sun, H.; Fan, W.; Xu, C.; Liu, Y.; Wang, H.; Hu, L.; Liang, Z.; Yu, L.; Lu, Y.; Kang, Z.; Zhang, Y. Graphdiyne-enabled interfacial transport sieving for efficient and sustainable carbon-based perovskite photovoltaics. *Energy Mater.* **2026**, *6*, 600165. https://dx.doi.org/10.20517/energymater.2026.309

**Received:** 8 Sep 2026
**First Decision:** 29 Sep 2026
**Revised:** 2 Nov 2026
**Accepted:** 11 Nov 2026
**Published:** 27 Nov 2026

**Academic Editors:**
Soo Young Kim, Hai Zhou
**Copy Editor:**
Ping Zhang
**Production Editor:**
Ping Zhang

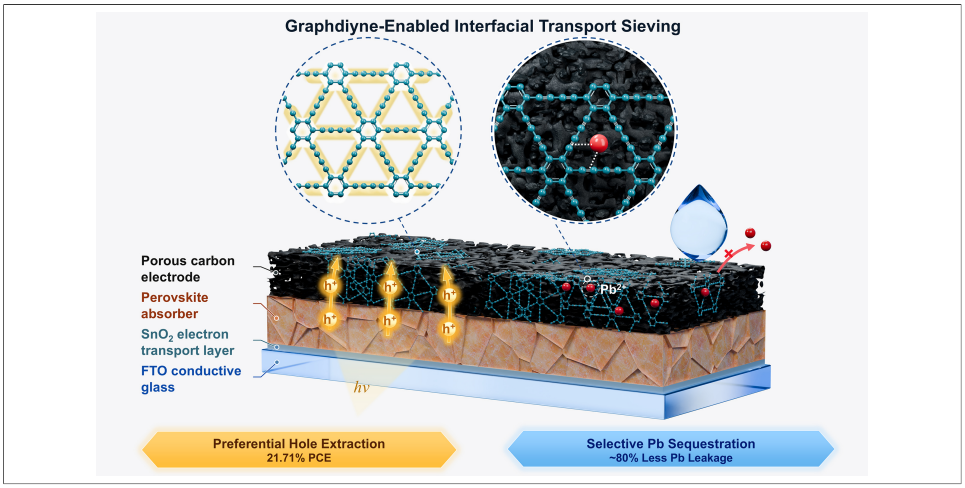


## Abstract

Sluggish hole extraction and toxic Pb leakage remain two critical barriers to carbon electrode-based perovskite solar cells (PSCs). Here, graphdiyne (GDY) is incorporated into the carbon electrode to establish an interfacial transport-sieving effect arising from differentiated electronic coupling and chemical affinity, enabling preferential hole transport while selectively retaining hazardous Pb species. The π-conjugated framework of GDY bridges the energy-level mismatch at the perovskite/carbon interface and provides an energetically favorable pathway for hole extraction. Meanwhile, its electron-rich π system, particularly the acetylenic π sites, interacts with undercoordinated $Pb^{2+}$ defects through π-electron coupling and interfacial charge redistribution, suppressing defect-related trap states and nonradiative recombination. Consequently, the space-charge-limited-current (SCLC)-derived effective hole mobility increases by approximately ninefold. Beyond its electronic functions, the abundant sp-hybridized acetylenic linkages strongly bind $Pb^{2+}$,

[1]Academy for Advanced Interdisciplinary Science and Technology, Beijing Key Laboratory for Advanced Energy Materials and Technologies, State Key Laboratory for Advanced Metals and Materials, University of Science and Technology Beijing, Beijing 100083, China.
[2]School of Materials Science and Engineering, Key Laboratory of Advanced Materials and Devices for Post-Moore Chips Ministry of Education, University of Science and Technology Beijing, Beijing 100083, China.
[#]These authors contributed equally to this work.

[*]**Correspondence to:** Prof. Zhuojian Liang, Prof. Zhuo Kang, Prof. Yue Zhang, Academy for Advanced Interdisciplinary Science and Technology, Beijing Key Laboratory for Advanced Energy Materials and Technologies, State Key Laboratory for Advanced Metals and Materials, University of Science and Technology Beijing, Beijing 100083, China; School of Materials Science and Engineering, Key Laboratory of Advanced Materials and Devices for Post-Moore Chips Ministry of Education, University of Science and Technology Beijing,

Beijing 100083, China. E-mail: zjliang@ustb.edu.cn; zhuokang@ustb.edu.cn; yuezhang@ustb.edu.cn

reducing lead leakage by up to 80%. Experimental analyses implicate the acetylenic motifs in Pb binding, while density functional theory (DFT) calculations identify the corner configuration of the acetylenic ring as the energetically preferred adsorption geometry. Leveraging this transport-selective interface, the optimized device achieves a champion power conversion efficiency (PCE) of 21.71% while enhancing operational and storage stability. These findings establish interfacial transport sieving as a promising strategy for efficient and environmentally responsible perovskite photovoltaics.

## INTRODUCTION

The remarkable progress of metal halide perovskites has driven perovskite solar cells (PSCs) toward their theoretical efficiency limit, shifting increasing attention toward scalability, durability, and environmental sustainability[1-3]. However, conventional high-performance PSCs commonly rely on expensive thermally evaporated Au/Ag electrodes and organic hole-transport layers (HTLs) containing hygroscopic dopants, thereby increasing fabrication costs and energy consumption while compromising long-term stability[4-7]. Carbon-contact PSCs that operate without a separate HTL offer a potentially simpler and less expensive alternative, with the added benefit of intrinsically stable electrode materials[8-10]. Their performance, however, is constrained by imperfect electronic contact between perovskite and carbon: weak interfacial coupling and mismatched energy levels slow hole extraction and increase recombination losses[11,12]. Meanwhile, toxic Pb leakage from damaged devices remains a critical environmental concern[13-15]. Accordingly, carbon electrode-based PSCs require an interface that can simultaneously facilitate efficient charge extraction and suppress the release of hazardous Pb species.

Considerable efforts have therefore been devoted to improving interfacial charge-transfer kinetics and mitigating Pb leakage. Lewis acids/bases[16-18], alkali-metal ions[19], and halide species[20] have been employed to passivate interfacial defects, tune energy-level alignment, and promote carrier extraction and transport. Functional polymers[21] and conjugated polymers[22], as well as two-dimensional materials such as graphene[23], MXenes[24], covalent organic frameworks[25], and phosphorene nanoribbons[26], have also been explored to regulate interfacial electronic structure and defect chemistry. Reduced-dimensional perovskites have likewise been introduced to suppress surface defects, optimize band alignment, and facilitate charge transfer[27]. In parallel, Pb-sequestration strategies relying on strong chemical binding have been developed using phosphonic-acid-containing molecules, thermally or ultraviolet-initiated polymerizable molecules, and mesoporous resins[28-31]. Nevertheless, these strategies generally address either electronic-transport losses or Pb immobilization, whereas their simultaneous regulation remains comparatively underexplored, particularly at the perovskite/carbon interface. These limitations highlight the need for a transport-selective interface that preferentially facilitates photogenerated-hole extraction while selectively retaining hazardous Pb species.

Graphdiyne (GDY) offers a distinctive platform for transport-selective interface engineering because its two-dimensional carbon network combines sp-hybridized linkages with $sp^2$-hybridized aromatic units[32-34]. Its extended π-conjugated framework and suitable electronic structure enable efficient electronic coupling and energetically favorable hole extraction[35,36], while the periodically distributed sp-hybridized acetylenic linkages furnish electron-rich π sites with strong affinity toward Pb species[37,38]. Importantly, these functionalities are intrinsically integrated within the same conjugated carbon framework rather than acting as independent structural motifs. The electron-rich π system, particularly the acetylenic π sites, can interact with undercoordinated $Pb^{2+}$ defects through π-electron coupling and interfacial charge redistribution, thereby attenuating defect-related trap states. Meanwhile, the acetylenic motifs can provide strong binding

sites for released Pb species. The coexistence of favorable electronic coupling and strong chemical affinity therefore provides a molecular basis for selectively promoting beneficial carrier transport while retaining hazardous Pb species.

Herein, we incorporate GDY into the carbon electrode to establish a graphdiyne-enabled interfacial transport-sieving effect in carbon electrode-based PSCs. Rather than relying on conventional size-exclusion mechanisms based on physical pore dimensions, this transport selectivity arises from species-dependent electronic coupling and chemical affinity at the perovskite/carbon interface. The π-conjugated framework of GDY bridges the energetic mismatch between the perovskite and carbon electrode, providing an energetically favorable pathway for hole extraction and increasing the space-charge-limited-current (SCLC)-derived effective hole mobility by approximately ninefold. Simultaneously, its electron-rich π system, particularly the acetylenic π sites, interacts with undercoordinated $Pb^{2+}$ defects through π-electron coupling and interfacial charge redistribution, thereby suppressing defect-related trap states and nonradiative recombination. Upon device damage, the sp-hybridized acetylenic sites further exhibit strong chemical affinity toward released Pb species, reducing Pb leakage by up to 80%; density functional theory calculations identify the corner sites of the acetylenic rings as the energetically preferred adsorption sites. Consequently, the optimized device achieves a champion power conversion efficiency (PCE) of 21.71% together with enhanced operational and storage stability. These results establish interfacial transport sieving as a design principle for reconciling preferential carrier transport with selective Pb retention in efficient and environmentally responsible perovskite photovoltaics.

## EXPERIMENTAL

### Materials

Patterned fluorine-doped tin oxide (FTO) glass (thickness, 2.2mm; sheet resistance, 15 Ω $sq^{-1}$) was obtained from Advanced Electron Technology Co., Ltd. An aqueous $SnO_2$ colloid (15 wt%) was obtained from Alfa Aesar. The perovskite precursors formamidinium iodide (FAI, 99.9%), methylammonium iodide (MAI, 99.9%), methylammonium chloride (MACl, 99.9%), and $PbI_2$ (99.999%) were supplied by Xi'an Yuri Solar Technology Co., Ltd. Sigma-Aldrich provided anhydrous N,N-dimethylformamide (DMF, 99.8%), dimethyl sulfoxide (DMSO, ≥ 99.9%), chlorobenzene (CB, 99.8%), acetone (99.8%), isopropanol (IPA, 99.5%), and lead(II) acetate (99.999%). The commercial DD-10 carbon paste, purchased from Guangzhou Saidi Technology Co., Ltd., contained graphite flakes and carbon black together with ethyl cellulose as the organic binder and terpineol as the solvent. Unless otherwise noted, the reagents were used without additional purification.

### Graphdiyne synthesis

GDY powder was synthesized via copper(II) acetate-mediated homocoupling of deprotected hexaethynylbenzene in pyridine, using a modified solution-phase synthesis protocol reported previously[39]. Copper(II) acetate (20 mg) was first introduced into pyridine (20 mL), and the mixture was sonicated for 5 min to promote dissolution. Separately, a three-neck flask was connected to an argon line maintained at approximately one bubble per second. The prepared copper acetate/pyridine solution was transferred to this flask, after which the deprotected hexaethynylbenzene monomer (20 mg) was introduced. The coupling was allowed to proceed for 24 h at room temperature under a continuous argon atmosphere. Formation of a black solid at the bottom of the flask signaled the appearance of the GDY product. Following vacuum filtration, the recovered material was washed with pyridine three times to remove residual copper acetate and then rinsed repeatedly with acetone to eliminate remaining organic residues. The collected black powder was dried under vacuum at 60 °C for 24 h. The final GDY yield was approximately 59%, calculated relative to the initial mass of hexaethynylbenzene.

## Device fabrication

Patterned FTO glass was successively cleaned with deionized water, ethanol, acetone, and IPA for 20 min and dried under a nitrogen stream. A 30 min UV-ozone treatment was then applied before coating. To form the $SnO_2$ electron-selective layer, the commercial colloid was diluted with deionized water at a dispersion-to-water volume ratio of 1:3, spun onto FTO at 3000 rpm for 30 s, and heated at 150 °C for 30 min. The perovskite absorber was formed by a sequential two-step deposition inside a nitrogen-filled glovebox in which both $H_2O$ and $O_2$ were maintained below 0.1 ppm. In the first step, $PbI_2$ (1.5 M) dissolved in DMF/DMSO (9:1, v/v) was coated onto $SnO_2$ at 1,500 rpm for 30 s and subsequently heated at 70 °C for 1 min. The second step involved spin-coating a 1 mL IPA solution containing FAI (90 mg), MAI (6.39 mg), and MACl (9 mg) at 2,000 rpm for 30 s. The deposited films were finally annealed at 150 °C for 15 min to complete the perovskite conversion.

GDY-containing carbon contacts were fabricated from commercial carbon paste after removal of its residual moisture and organic solvents by heating at 120 °C for 10 h. GDY was then blended with the dried paste to obtain nominal loadings of 0, 3, 6, and 9 wt%; each percentage refers to the GDY mass divided by the combined mass of GDY and dried carbon paste. For each composition, 4.5 g of the mixture was placed in a ball-milling jar with zirconia balls (5 mm diameter; ball-to-powder mass ratio, 10:1), and chlorobenzene (10 mL) was added as the dispersion medium. Milling was conducted at 300 rpm for 12 h to prepare the carbon slurry. The resulting formulations were doctor-bladed onto the perovskite surface and held at 100 °C for 30 min to produce the carbon electrodes. The 6 wt% GDY/carbon formulation served as the optimized contact in subsequent measurements unless a different loading is explicitly indicated.

## Characterization

Photovoltaic current density-voltage (*J-V*) measurements were made with a Keithley 2450 source meter under simulated Air Mass 1.5 Global (AM 1.5G) sunlight from an ENLITECH SS-X100R system (100 mW $cm^{-2}$); irradiance was calibrated against a silicon reference cell. Both voltage-sweep directions were recorded at 25 °C using a scan rate of 0.02 V $s^{-1}$ and a 10 ms delay. For devices with a nominal area of 0.1 $cm^2$, the illuminated area was defined by a 0.07208 $cm^2$ shadow-mask aperture. Open-circuit voltage ($V_{OC}$) was also measured as a function of light intensity, adjusted from 0.02 to 1 sun by the SS-X100R's integrated neutral-density filter wheel. External quantum efficiency (EQE) was determined with an Enlitech QE-R3011 system operating in alternating current (AC) mode under monochromatic excitation and referenced to a standard silicon cell.

Microstructural examination comprised surface and cross-sectional field-emission scanning electron microscopy (FESEM, FEI QUANTA 3D; accelerating voltage, 5 kV) and ambient atomic force microscopy (AFM, Bruker Dimension Icon). For AFM, a Pt/Ir-coated SCM-PIT probe with a nominal spring constant of 2.8 N $m^{-1}$ was employed. Raman data were obtained at room temperature on a Horiba Jobin Yvon HR800 confocal microscope using a 532 nm excitation beam. An Edinburgh Instruments FLS1000 spectrometer was used for steady-state photoluminescence (PL) and time-resolved PL (TRPL). Steady-state emission was excited from the perovskite side at 475 nm with a 450 W xenon arc lamp. TRPL excitation was supplied by an EPL-475 pulsed diode laser (20 nJ $cm^{-2}$, 1 MHz), and the emission was monitored at 800 nm. Transient photocurrent (TPC) and transient photovoltage (TPV) were acquired using the measurement setup at the Institute of Physics, Chinese Academy of Sciences. A 532 nm pulsed laser (Opotek RADIANT 532 LD, 20 Hz) excited the devices, and a Tektronix MDO3034 digital oscilloscope captured the decays at input impedances of 50 Ω for TPC and 1 MΩ for TPV. A Nanjing Hongzhao S3000 light-emitting diode (LED) source provided adjustable background illumination. Fourier-transform infrared (FTIR) spectra were acquired in diamond-crystal attenuated-total-reflectance mode on a Bruker Tensor-27 instrument, with 0.5 $cm^{-1}$ resolution and 64 accumulated scans.

Ultraviolet photoelectron spectroscopy (UPS) was performed with a PHI 5000 VersaProbe III analyzer using He I photons (21.22 eV) and a -9.0 V bias applied to the sample. A sputter-cleaned Au reference provided the Fermi-edge calibration ($E_F$ = 0 eV), and all reported binding energies were corrected for the sample bias. X-ray photoelectron spectra (XPS) were collected on a Thermo Fisher Scientific ESCALAB 250Xi equipped with monochromatic Al Kα radiation (1,486.6 eV). The high-resolution scans used a pass energy of 20 eV, with a low-energy dual-beam flood gun compensating for sample charging; the C 1s signal at 284.8 eV served as the binding-energy reference. Peak deconvolution employed a Shirley background and Gaussian-Lorentzian product profiles (30% Lorentzian contribution). For the Pb 4f doublet, the spin-orbit separation and integrated-area ratio were constrained to 4.86 eV and 4:3 (Pb $4f_{7/2}$:Pb $4f_{5/2}$), respectively. The $PbI_2$+GDY specimen was prepared by sonicating a 1:1 mass mixture of $PbI_2$ and GDY in chlorobenzene for 30 min, drop-casting the dispersion onto a Si wafer, and vacuum-drying at 70 °C for 2 h.

Capacitance-voltage (*C-V*) and electrochemical impedance spectroscopy (EIS) were carried out in the dark using a CS310MA electrochemical workstation. The *C-V* sweep spanned -0.2 to 1.2 V relative to the open-circuit potential, with a 5 kHz probing frequency and a 0.01 V AC excitation. For EIS, a 0.02 V AC perturbation was applied over 100 kHz to 0.1 Hz. Dissolved Pb in aqueous samples was quantified by inductively coupled plasma mass spectrometry (ICP-MS, Agilent 7800). Operational tests following ISOS-L-1 [International Summit on Organic Photovoltaic Stability light-soaking protocol (level 1)] were conducted on unencapsulated devices in an environmental chamber, with continuous white-LED illumination at an intensity equivalent to approximately 1 sun and maximum-power-point (MPP) tracking throughout. Storage stability was evaluated following the ISOS-D-1 [International Summit on Organic Photovoltaic Stability dark-storage protocol (level 1)] protocol. Unencapsulated devices were stored in the dark under open-circuit conditions in a temperature- and humidity-controlled chamber (23 ± 4 °C, 35 ± 5% relative humidity) in ambient air. Photovoltaic performance was measured under simulated AM 1.5G illumination at 0 h (initial) and after 50, 100, 150, 200, 300, 400, 500, 600, 750, 900, 1,050, 1,200, 1,350, 1,500, 1,650, 1,800, and 2,000 h of storage. PCE retention was calculated as PCE (*t*)/PCE (0) × 100%, where PCE (*t*) and PCE (0) represent the PCE measured at time t and the initial PCE, respectively.

## Computational methods

First-principles calculations were carried out in the Vienna ab initio Simulation Package (VASP) using the projector-augmented-wave (PAW) treatment of electron-ion interactions[40,41]. A kinetic-energy cutoff of 400 eV was imposed on the plane-wave basis. The Perdew-Burke-Ernzerhof (PBE) exchange-correlation functional within the generalized gradient approximation was adopted for geometry optimization, while the electronic structures were evaluated with the Heyd-Scuseria-Ernzerhof (HSE06) hybrid functional. Atomic positions were optimized by the conjugate-gradient method until all residual forces were smaller than 0.02 eV $Å^{-1}$. Electronic self-consistency was required to reach $10^{-5}$ eV.

For the slab models, Brillouin-zone sampling employed a Γ-centered 2 × 2 × 1 Monkhorst-Pack k-point mesh. The $FAPbI_3$ (001) slab comprised two layers of $PbI_6$ octahedra, terminated by $PbI_2$, with an undercoordinated $Pb^{2+}$ site introduced at the surface. More than 15 Å of vacuum separated adjacent slab images along the surface normal, where a dipole correction was also applied. GDY adsorption and electronic-structure analyses used a monolayer GDY unit cell with an optimized lattice constant of 9.460 Å; a 20 Å vacuum region was included perpendicular to the sheet to reduce spurious interactions between periodic replicas[42]. To assess the spatial character of the frontier states, the valence-band-maximum (VBM) Kohn-Sham wavefunctions were extracted and visualized for both the Pb-defective $FAPbI_3$ surface and its GDY-modified counterpart.

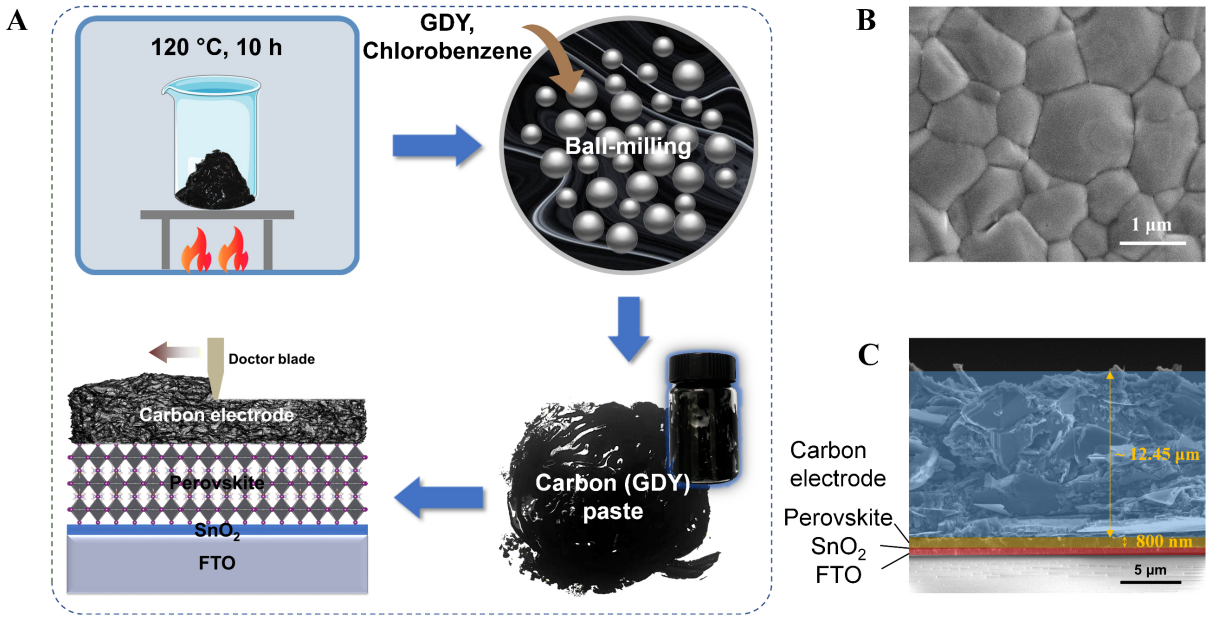


**Figure 1.** (A) Schematic illustration of the preparation of GDY-modified carbon electrode; (B) Top-view SEM image of perovskite film; (C) Cross-section SEM image of PSC. GDY: Graphdiyne; PSC: perovskite solar cell; FTO: fluorine-doped tin oxide; SEM: scanning electron microscopy.

## RESULTS AND DISCUSSION

GDY was synthesized through a $Cu^{2+}$-catalyzed acetylenic coupling reaction of hexaethynylbenzene[32,43]. Its expected framework, shown in Supplementary Figure 1, contains aromatic $sp^2$-carbon units linked by sp-carbon diyne segments. Raman spectroscopy provides supporting structural evidence [Supplementary Figure 2]. The signals at 1,325 and 1,586 $cm^{-1}$ correspond to the disorder-related D mode of the $sp^2$ carbon rings and the in-plane G mode of the conjugated carbon domains, respectively. Two additional features at 1,928 and 2,217 $cm^{-1}$ are assigned to vibrations of the conjugated diyne linkages, confirming the coexistence of sp-carbon motifs within the GDY network[43].

Figure 1A summarizes the fabrication route for the GDY-containing carbon contact. Commercial carbon paste was first heated at 120 °C for 10 h to remove the original solvent, after which GDY was introduced at 0, 3, 6, and 9 wt%. The mixtures were redispersed in chlorobenzene and ball-milled for 12 h, followed by doctor-blade coating and a 30 min treatment at 100 °C. The underlying perovskite absorber was prepared by sequential two-step deposition. Top-view scanning electron microscopy (SEM) and AFM images show a compact and smooth perovskite surface with large grains [Figure 1B and Supplementary Figure 3], while the cross-sectional microscopy confirms the FTO/$SnO_2$/perovskite/carbon stack architecture [Figure 1C]. Incorporating GDY into the carbon contact therefore provides a direct route to regulate the perovskite/carbon interface without introducing an additional interlayer.

To clarify the carrier-transport branch of the proposed interfacial transport-sieving effect, UPS was used to determine the energetic positions on separately prepared thin films of the perovskite, GDY, and different carbon electrodes. Figure 2A presents the secondary-electron cutoff ($E_{cutoff}$) and valence-band-edge regions ($E_{onset}$). The work function ($\Phi$) was calculated as $\Phi = h\nu - E_{cutoff}$ ($h\nu$ = 21.22 eV, He I), and the VBM as $E_{VBM} = -(\Phi + E_{onset})$, with $E_{onset}$ obtained by linear extrapolation of the valence-band edge to the baseline. For perovskite, $E_{cutoff}$ = 16.77 eV and $E_{onset}$ = 1.06 eV yield $\Phi$ = 4.45 eV and $E_{VBM}$ = -5.51 eV. Combined with the EQE-derived bandgap of 1.55 eV [Supplementary Figure 4], the estimated conduction-band minimum is

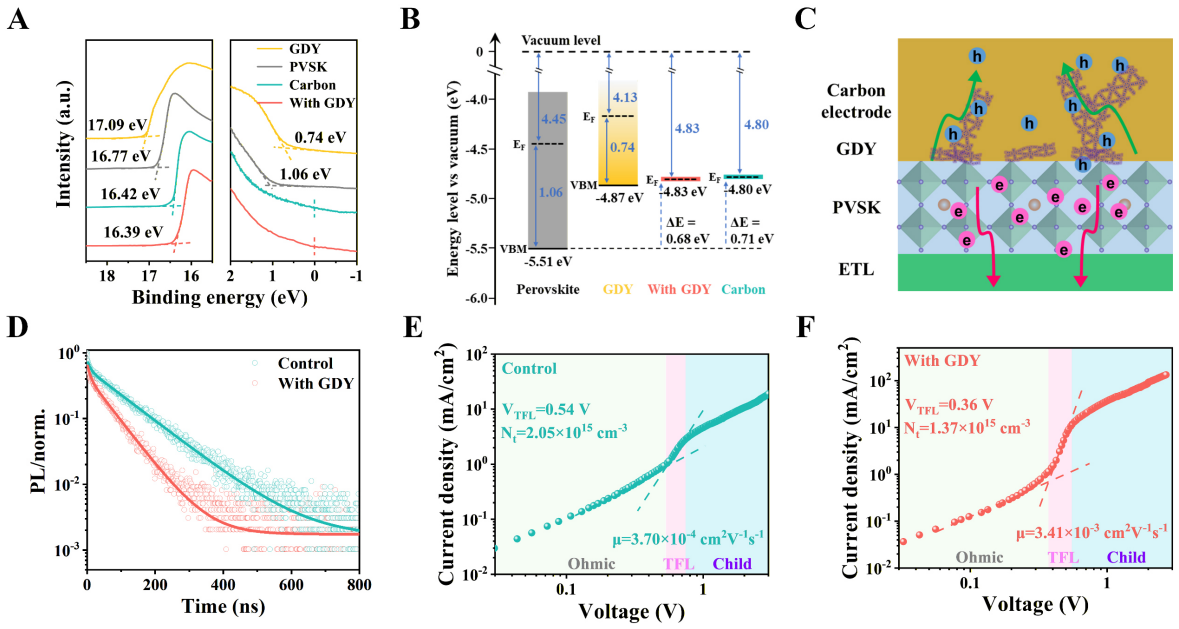


**Figure 2.** (A) UPS spectra of GDY, perovskite film, and different carbon electrodes; (B) Energy-level diagram for interfacial hole transfer; (C) Schematic diagram of photogenerated carrier transport via GDY as a hole-transfer pathway; (D) TRPL decay curves of perovskite devices without and with GDY modification; Dark *J-V* curves of hole-only devices (E) without and (F) with GDY modification. UPS: Ultraviolet photoelectron spectroscopy; GDY: graphdiyne; PL: photoluminescence; TRPL: time-resolved PL; *J-V*: current density-voltage; PVSK: perovskite; ETL: electron transport layer; TFL: trap-filled-limit.

-3.96 eV [Figure 2B]. The cutoff energies of pristine carbon (16.42 eV) and 6 wt% GDY/carbon (16.39 eV) correspond to work functions of 4.80 and 4.83 eV, respectively, reducing the nominal energetic offset between the perovskite VBM and electrode Fermi level from 0.71 to 0.68 eV. More importantly, GDY exhibits a VBM of -4.87 eV, positioned between the perovskite VBM and the carbon Fermi level, generating a more graded energetic landscape for hole extraction [Figure 2C]. Rather than constituting a geometric sieve, GDY therefore provides an electronically favorable interfacial pathway that preferentially promotes photogenerated-hole transfer toward the carbon electrode.

Steady-state PL and TRPL measurements were subsequently performed on FTO/perovskite/carbon contacts to probe the effect of GDY on charge separation behavior. The GDY-containing contact shows marked PL quenching relative to the control [Supplementary Figure 5], which suggests that the photogenerated holes can be more efficiently transported from perovskite to carbon layer. Besides, TRPL was conducted to further verify the above conclusion. As seen in Figure 2D, the device with GDY modification shows a faster PL decay curve. The decay curves were fitted using a biexponential function[44]:

$$I(t) = A_1 \exp\left(-\frac{t}{\tau_1}\right) + A_2 \exp\left(-\frac{t}{\tau_2}\right) \quad (1)$$

The average PL lifetime decreases from 109.29 ns for the control to 63.74 ns after GDY incorporation [Supplementary Table 1]. In the presence of an extracting carbon contact, the combined PL quenching and shortened lifetime are consistent with more rapid interfacial carrier extraction, particularly when considered together with the UPS-derived energetic alignment.

To further elucidate the influence of GDY on hole transport at the perovskite/carbon contact, SCLC analysis was conducted using hole-only structures [FTO/poly(3,4-ethylenedioxythiophene):poly(styrenesulfonate) (PEDOT:PSS)/perovskite/carbon]. The corresponding dark *J-V* curves are plotted on a logarithmic scale in Figure 2E and F. Three bias-dependent responses can be distinguished: an approximately linear Ohmic

regime at low voltage, a steep current rise associated with trap filling at intermediate voltage, and a high-bias region described by Child's law. The trap-filled-limit voltage ($V_{TFL}$) is determined from the transition between the Ohmic and trap-filled-limit (TFL) regimes, from which the apparent trap density ($N_t$) can be estimated according to[45]:

$$N_t = \frac{2\varepsilon\varepsilon_0 V_{TFL}}{qL^2} \tag{2}$$

where $\varepsilon = 22$ is the assumed relative permittivity of perovskite; $\varepsilon_0 = 8.85 \times 10^{-12}$ F m$^{-1}$ is the vacuum permittivity; $q = 1.6 \times 10^{-19}$ C is the elementary charge; and $L = 800$ nm is the absorber thickness. The GDY-modified device exhibits a substantially lower $V_{TFL}$ of 0.36 V than the control device (0.54 V), corresponding to a decrease in the apparent trap density from $2.05 \times 10^{15}$ cm$^{-3}$ for the reference to $1.37 \times 10^{15}$ cm$^{-3}$ after GDY introduction. This reduction is consistent with the suppression of electrically active trap states upon GDY incorporation. As discussed below, the electron-rich π-conjugated framework of GDY, particularly its acetylenic π sites, can interact with undercoordinated $Pb^{2+}$ defects through π-electron coupling and interfacial charge redistribution, thereby attenuating defect-related electronic states and associated trapping losses.

In the Child's-law region (above 1.0 V), the current density is proportional to the square of the applied voltage, allowing the SCLC-derived effective hole mobility to be estimated using the Mott-Gurney relation[46]:

$$J = \frac{9\varepsilon\varepsilon_0\mu V^2}{8L^3} \tag{3}$$

where $J$ is the dark current density, $\mu$ is the SCLC-derived effective hole mobility, and $V$ is the applied voltage. Upon GDY incorporation, the SCLC-derived effective hole mobility increases markedly from $3.70 \times 10^{-4}$ cm$^2$ V$^{-1}$ s$^{-1}$ for the control device to $3.41 \times 10^{-3}$ cm$^2$ V$^{-1}$ s$^{-1}$ for the GDY-modified device, corresponding to an approximately ninefold enhancement. Future work will compute the direction-resolved effective masses and carrier mobilities of the GDY/perovskite heterostructure using the Boltzmann transport formalism, to quantitatively link the observed electronic-structure changes to the experimentally measured mobility enhancement[47,48]. These results indicate that the π-conjugated GDY framework establishes an energetically favorable transport pathway while mitigating trap-assisted losses, thereby supporting the preferential hole-transport branch of the interfacial transport-sieving effect.

The influence of GDY on charge accumulation and recombination was next examined by capacitance-voltage analysis. Mott-Schottky plots measured at 5 kHz are shown in Figure 3A. The apparent carrier density ($N_A$) was estimated from the slope of the $C^{-2}$-V response using[49]:

$$N_A(x) = -\frac{2}{q\varepsilon\varepsilon_0}\left(\frac{dC(x)^{-2}}{dV}\right)^{-1} \tag{4}$$

The slopes of the Mott-Schottky plots are $-9.15 \times 10^{13}$ and $-1.14 \times 10^{14}$ (F/cm$^2$)$^{-2}$ V$^{-1}$ for the control and GDY-modified devices, respectively, corresponding to calculated $N_A$ of $7.02 \times 10^{16}$ cm$^{-3}$ and $5.63 \times 10^{16}$ cm$^{-3}$. The Mott-Schottky-derived carrier density represents an apparent rather than intrinsic bulk carrier density, given possible contributions from geometric capacitance, carrier injection, interfacial polarization, and ionic redistribution. Nonetheless, the reduced Mott-Schottky-derived apparent carrier density suggests a change in the interfacial electrostatic response after GDY incorporation. Together with the TPC/TPV and dark-current results, this behavior is consistent with alleviated interfacial charge accumulation and recombination. Flat-band potential ($V_{FB}$) was also obtained by extending the fitting line of the linear part of the curve to the x-axis. The PSCs with GDY exhibited a higher $V_{FB}$ of 0.778 V compared with 0.750 V for the control PSCs, consistent with an increased built-in potential, which may facilitate charge separation and contribute to the enhanced $V_{OC}$[50-52]. In addition, the GDY-modified PSC exhibits a lower dark current density

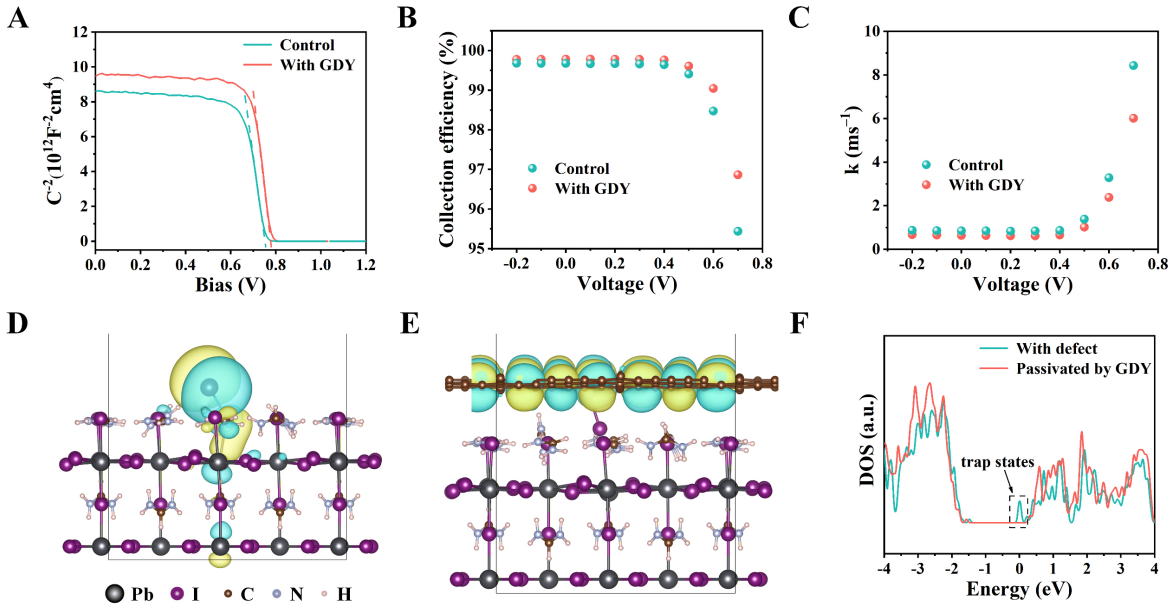


**Figure 3.** (A) Mott-Schottky analysis of PSCs without and with GDY modification measured at 5 kHz; (B) Charge-collection efficiency and (C) recombination rate derived from TPC and TPV measurements under different bias voltages; Spatial distributions of the VBM Kohn-Sham wavefunctions for (D) an undercoordinated $Pb^{2+}$ defect and (E) the corresponding GDY-modified configuration. The yellow and cyan isosurfaces represent the positive and negative signs of the displayed wavefunction component, respectively. The black, purple, brown, cyan, and pink spheres denote Pb, I, C, N, and H, respectively; (F) DOS of the defective perovskite and the corresponding GDY-modified model. PSCs: Perovskite solar cells; GDY: graphdiyne; TPC: transient photocurrent; TPV: transient photovoltage; VBM: valence-band-maximum; DOS: density of states.

[Supplementary Figure 6], which further agrees with diminished leakage and recombination losses, thus contributing to the improved $V_{OC}$ and fill factor (FF)[53].

Light-intensity-dependent $V_{OC}$ measurements provide an additional probe of trap-assisted recombination. The data in Supplementary Figure 7 were analyzed according to[54]:

$$V_{OC} = nkT\ln(I)/q + \text{constant} \quad (5)$$

where $n$, $k$, $T$, and $I$ represent the ideality factor, Boltzmann constant, absolute temperature, and incident light intensity, respectively. The extracted $n$ decreases from 1.60 for the reference to 1.48 for the GDY-modified device, suggesting a reduced contribution from trap-assisted nonradiative recombination.

To further elucidate the charge-transport and recombination dynamics, modulated TPC and modulated TPV were measured to get a deeper insight into charge transport and recombination processes within the devices[55]. The TPC and TPV decay time constants ($\tau_C$ and $\tau_V$, respectively) were extracted by fitting the decay portions of the corresponding transient curves at different bias voltages using a single-exponential decay function [Supplementary Figures 8 and 9]. The fitted values are summarized in Supplementary Tables 2 and 3, respectively. The TPC decay is faster for the GDY-containing device over the investigated bias range [Supplementary Figure 8 and Supplementary Table 2], consistent with more rapid charge extraction. In contrast, the TPV decay is prolonged after GDY incorporation [Supplementary Figure 9 and Supplementary Table 3], indicating slower photovoltage decay and reduced recombination. The charge-collection efficiency ($\eta_{coll}$) was calculated from $\eta_{coll} = 1 - \tau_C/\tau_V$, with $\tau_C$ and $\tau_V$ expressed in consistent time units [Supplementary Table 4]. As summarized in Figure 3B, the GDY-containing device exhibits a higher $\eta_{coll}$ across the investigated bias range, demonstrating a more efficient charge extraction and transport process within the

target device, thereby contributing to the enhanced $V_{OC}$ and $J_{SC}$. The interfacial recombination rate ($k_r$), estimated as $k_r = 1/\tau_V$, is correspondingly lower [Figure 3C]. Together, these transient measurements support accelerated extraction accompanied by suppressed trap-mediated recombination.

To identify the microscopic origin of the reduced defect activity, density functional theory (DFT) calculations were carried out for a representative $FAPbI_3$ crystal model containing an undercoordinated $Pb^{2+}$ defect [Supplementary Figure 10]. The VBM Kohn-Sham wavefunction of the defective perovskite exhibits pronounced spatial localization around the Pb center [Figure 3D]. When GDY is brought into contact with the defective surface, its electron-rich π-conjugated network, particularly the acetylenic π sites, interacts electronically with the undercoordinated $Pb^{2+}$ center. This interaction leads to a markedly more delocalized VBM wavefunction across the GDY/perovskite interface [Figure 3E and Supplementary Figure 11], accompanied by substantial suppression of the defect-related density of states (DOS) feature [Figure 3F][56]. These simulation results therefore support a defect-passivation mechanism based on π-electron coupling and interfacial charge redistribution. By reducing the electronic localization associated with the undercoordinated-Pb defect, GDY suppresses trap-mediated nonradiative recombination while preserving the extended π network required for carrier transport.

The second branch of interfacial transport sieving concerns the selective retention of hazardous Pb species after device damage. Owing to the electron-rich and chemically accessible acetylenic motifs within GDY, the modified carbon electrode is expected to provide high-affinity binding sites for released Pb species. To evaluate this function at the device level, control and GDY-modified PSCs (1 $cm^2$ carbon electrode on 2.25 $cm^2$ perovskite film) were mechanically fractured using ceramic tweezers [Supplementary Figure 12] and immersed in 50 mL of deionized water (pH 6.8) at 25 ± 1 °C [Figure 4A]. The total Pb content per device is ca. 240 μg, and the GDY loading is ca. 0.22 mg. The Pb concentration evolution process in the surrounding water was monitored by ICP-MS. As shown in Figure 4B, Pb release increases rapidly during the first ~50 min and approaches a plateau after ~100 min. At the end of the measurement, the Pb concentration reaches approximately 2.53 ppm for the control device but only 0.47 ppm for the GDY-modified device, corresponding to an approximately 80% reduction in Pb leakage. $Pb^{2+}$ test strips provide the same qualitative trend [Supplementary Figure 13]. Measurements performed on eight devices per condition further reproduce the markedly lower Pb concentration for GDY-containing devices [Figure 4C], demonstrating that the Pb-retention effect is reproducible rather than arising from a single-device fluctuation. We further evaluated Pb leaching under simulated acid rain conditions (pH 4.5, adjusted with dilute $HNO_3$) following mechanical impact. After 150 min of immersion in simulated acid rain, the Pb concentration reached 2.86 ppm for the control device, compared to only 0.69 ppm for the GDY-modified device [Supplementary Figure 14]. This confirms that GDY retains its Pb-sequestration capability under acidic conditions even after mechanical damage. Pb-loaded electrodes should be collected as lead-containing hazardous waste, following standard Pb-pollution remediation protocols. GDY's strong binding affinity for Pb also facilitates subsequent recovery and recycling.

The Pb-binding capability of the GDY-containing carbon electrode was further examined independently of the complete device. Carbon films without and with GDY were immersed in a 10 ppm $Pb^{2+}$ solution for 10 min, washed with deionized water, and dried. Elemental mapping by energy-dispersive X-ray spectroscopy reveals only a weak Pb signal on the pristine carbon film but a substantially stronger and more spatially distributed Pb signal after GDY incorporation [Supplementary Figure 15]. Consistently, XPS detects clear Pb 4f signals on the GDY-containing carbon film after immersion, whereas the corresponding signal on pristine carbon remains weak [Supplementary Figure 16]. These observations demonstrate that GDY introduces additional Pb-binding sites into the carbon electrode. Sorption kinetics and isotherm measurements were then used to quantify the intrinsic $Pb^{2+}$-binding capability of GDY. As shown in

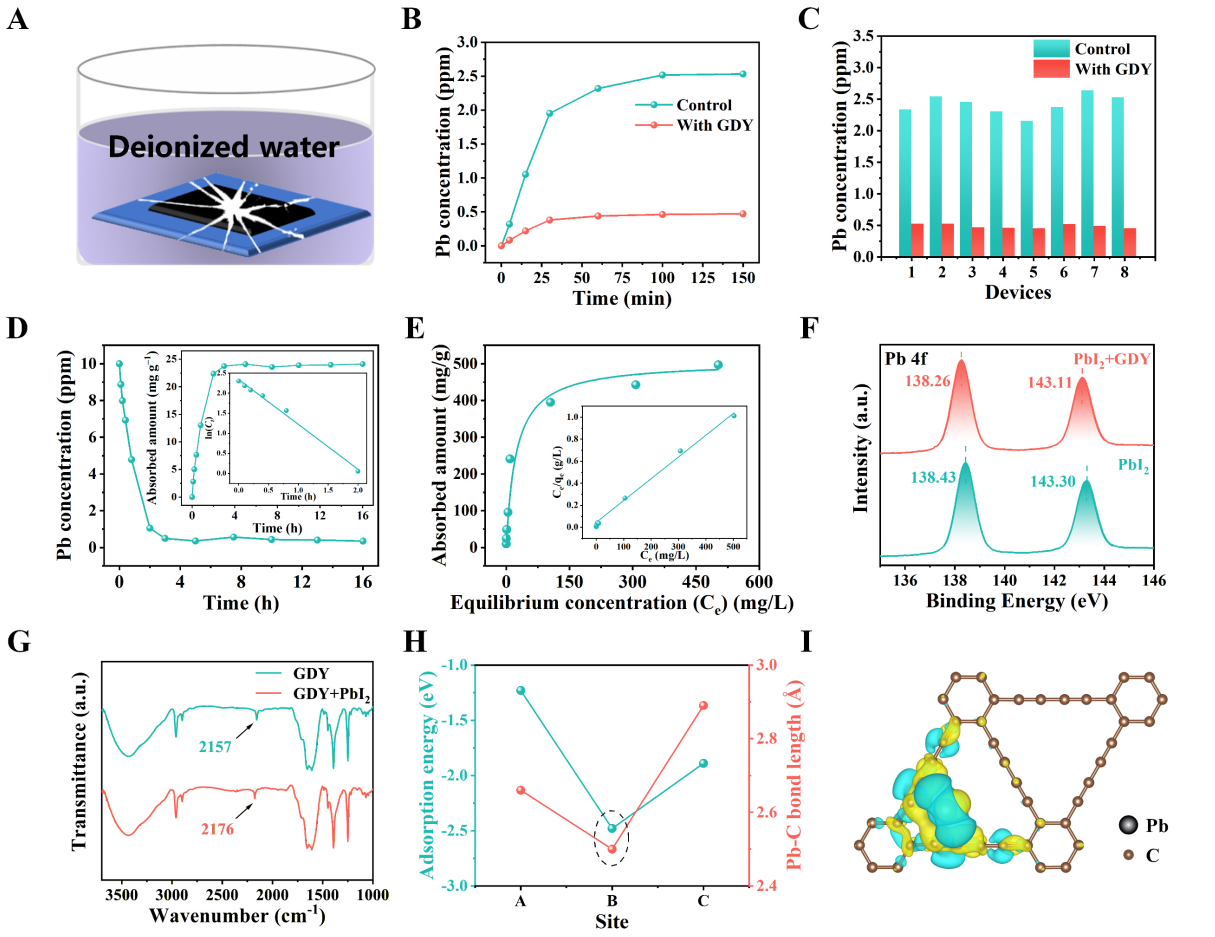


**Figure 4.** (A) Schematic diagram of Pb leakage test; (B) Time-dependent Pb concentration in deionized water after immersion of mechanically damaged PSCs at 25 ± 1 °C (ambient temperature); (C) Pb concentration measured for eight devices per condition; (D) $Pb^{2+}$ sorption kinetics of GDY at an initial $Pb^{2+}$ concentration of 10.0 ppm; the insets show the adsorbed amount and apparent first-order kinetic analysis; (E) Langmuir sorption isotherm of $Pb^{2+}$ on GDY; The inset is the linearized Langmuir fit; (F) Pb 4f XPS spectra of $PbI_2$ and $PbI_2$+GDY; (G) FTIR spectra of GDY and GDY+$PbI_2$; (H) Calculated adsorption energies and Pb-C bond lengths for three Pb adsorption configurations on GDY; (I) Charge-density difference map for the preferred Pb/GDY configuration. Yellow and cyan isosurfaces denote charge accumulation and charge depletion, respectively, at isovalues of ±0.001 e $Å^{-3}$. PSCs: Perovskite solar cells; GDY: graphdiyne; XPS: X-ray photoelectron spectra; FTIR: Fourier-transform infrared.

Figure 4D and Supplementary Note 1, the $Pb^{2+}$ concentration decreases from 10 ppm to near the detection baseline within the first 3 h, and more than 95% of $Pb^{2+}$ is removed at equilibrium. The rapid initial $Pb^{2+}$ uptake can be empirically described by an apparent first-order concentration-decay model, yielding $k_{app}$ = 1.12 $h^{-1}$. Langmuir analysis further yields an apparent maximum $Pb^{2+}$ sorption capacity of 508 mg $g^{-1}$ for GDY powder [Figure 4E and Supplementary Note 2]. Together with the rapid $Pb^{2+}$ uptake and high distribution coefficient, these results demonstrate the substantial Pb-binding capability of GDY and provide a quantitative basis for the reduced leakage observed at the device level.

Spectroscopic measurements were used to identify the structural motifs involved in Pb binding. The Pb $4f_{7/2}$ and Pb $4f_{5/2}$ peaks of $PbI_2$ are located at 138.43 and 143.30 eV, respectively, and shift to 138.26 and 143.11 eV after interaction with GDY [Figure 4F]. The downshift indicates a changed electronic environment of Pb and is consistent with interfacial charge redistribution upon Pb-GDY binding. The spectral changes support detectable interfacial electronic coupling between Pb species and the electron-rich sp-hybridized acetylenic sites of GDY, which provides a microscopic basis for the selective retention of Pb species within the transport-sieving interface. FTIR spectroscopy provides complementary evidence: the conjugated

-C≡C-C≡C- stretching band shifts from 2,157 $cm^{-1}$ for pristine GDY to 2,176 $cm^{-1}$ after $PbI_2$ exposure [Figure 4G]. This frequency shift demonstrates that the local vibrational and electronic environment of the acetylenic linkage is perturbed by Pb binding, supporting direct involvement of the acetylenic units in the interaction[57].

DFT calculations were further used to compare three representative adsorption configurations for a Pb atom on GDY [Supplementary Figure 17]. After structural relaxation, all three configurations exhibit local distortion of the GDY framework, reflecting appreciable Pb-GDY interaction[58]. The adsorption energy was calculated as $E_{ads} = E_{(Pb+GDY)} - E_{(GDY)} - E_{(Pb)}$, where $E_{(Pb+GDY)}$ is the total energy of the Pb-adsorbed GDY system, $E_{(GDY)}$ is the energy of the pristine GDY monolayer, and $E_{(Pb)}$ is the energy of an isolated Pb atom in a cubic box. The calculated adsorption energies for sites A, B, and C are -1.23, -2.48, and -1.89 eV, respectively [Figure 4H]. The B configuration, located at the corner of the acetylenic ring, therefore has the most negative adsorption energy and also exhibits the shortest Pb-C distance, identifying this position as the energetically preferred binding configuration. The charge-density-difference map for the B configuration [Figure 4I] shows noticeable electron redistribution around the Pb/GDY contact, consistent with the XPS and FTIR evidence for strong electronic coupling. Although the atomistic model uses an isolated neutral Pb atom as a simplified adsorbate (real leached Pb species include hydrated $Pb^{2+}$, $PbI_2$, and $PbI_3^-$ complexes), these calculations aim to qualitatively identify the preferred binding geometry and the electronic nature of the interaction rather than to quantitatively predict absolute adsorption energies. The combined experimental and theoretical results consistently identify the acetylenic region of GDY as the dominant high-affinity motif for Pb sequestration.

The photovoltaic performance of this dual interfacial function was finally evaluated using devices containing different GDY loadings. Figure 5A compares the best-performing *J-V* curves, with the corresponding photovoltaic parameters given in Supplementary Table 5. The 6 wt% GDY device delivers the highest PCE of 21.71%, with $J_{SC}$ = 24.71 mA $cm^{-2}$, $V_{OC}$ = 1.128 V, and FF = 77.9%, compared with 17.89% for the control device ($J_{SC}$ = 24.32 mA $cm^{-2}$, $V_{OC}$ = 1.093 V, and FF = 67.3%). The simultaneous increases in $V_{OC}$ and FF are consistent with reduced recombination losses and more favorable interfacial hole extraction. The reduced hysteresis upon GDY incorporation suggests more efficient and balanced charge extraction, consistent with the improved interfacial contact and reduced defect density at the perovskite/carbon interface [Supplementary Figure 18]. Statistical analysis of 40 devices per group ($n$ = 40 for each condition) [Figure 5B] shows the average PCE increases from 17.05 ± 0.47% for the control devices to 20.92 ± 0.35% for the GDY-modified devices, with both a higher mean performance and a narrower PCE distribution after GDY incorporation, indicating improved device reproducibility. The integrated $J_{SC}$ values derived from EQE spectra are 24.61 and 24.20 mA $cm^{-2}$ for the GDY-modified and control devices, respectively [Figure 5C], in close agreement with the corresponding *J-V* measurements. To evaluate the scalability of the GDY-modified carbon electrode, we further fabricated 1 $cm^2$ devices and measured their *J-V* characteristics [Supplementary Figure 19]. The optimal 1 $cm^2$ GDY-modified device achieved a champion PCE of 18.39% under reverse scan.

The electrical response of the contacts was further probed by impedance spectroscopy at 0.8 V in the dark [Figure 5D]. Two features in the Nyquist spectra were assigned, using the stated equivalent-circuit model, to transport resistance ($R_{tr}$) at high frequency and recombination resistance ($R_{rec}$) at lower frequency. As summarized in Supplementary Table 6, the GDY-modified device exhibits a lower $R_{tr}$ of 673 Ω than the control device (867 Ω), indicating facilitated interfacial charge extraction and transport. Meanwhile, $R_{rec}$ increases from 435 to 899 Ω, suggesting suppressed charge recombination after GDY incorporation. These results are consistent with the improved energetic alignment and carrier-transport characteristics discussed above, further supporting preferential hole transport at the GDY-modified perovskite/carbon interface. Charge collection was also examined by plotting the photocurrent density ($J_{ph}$) against the effective voltage

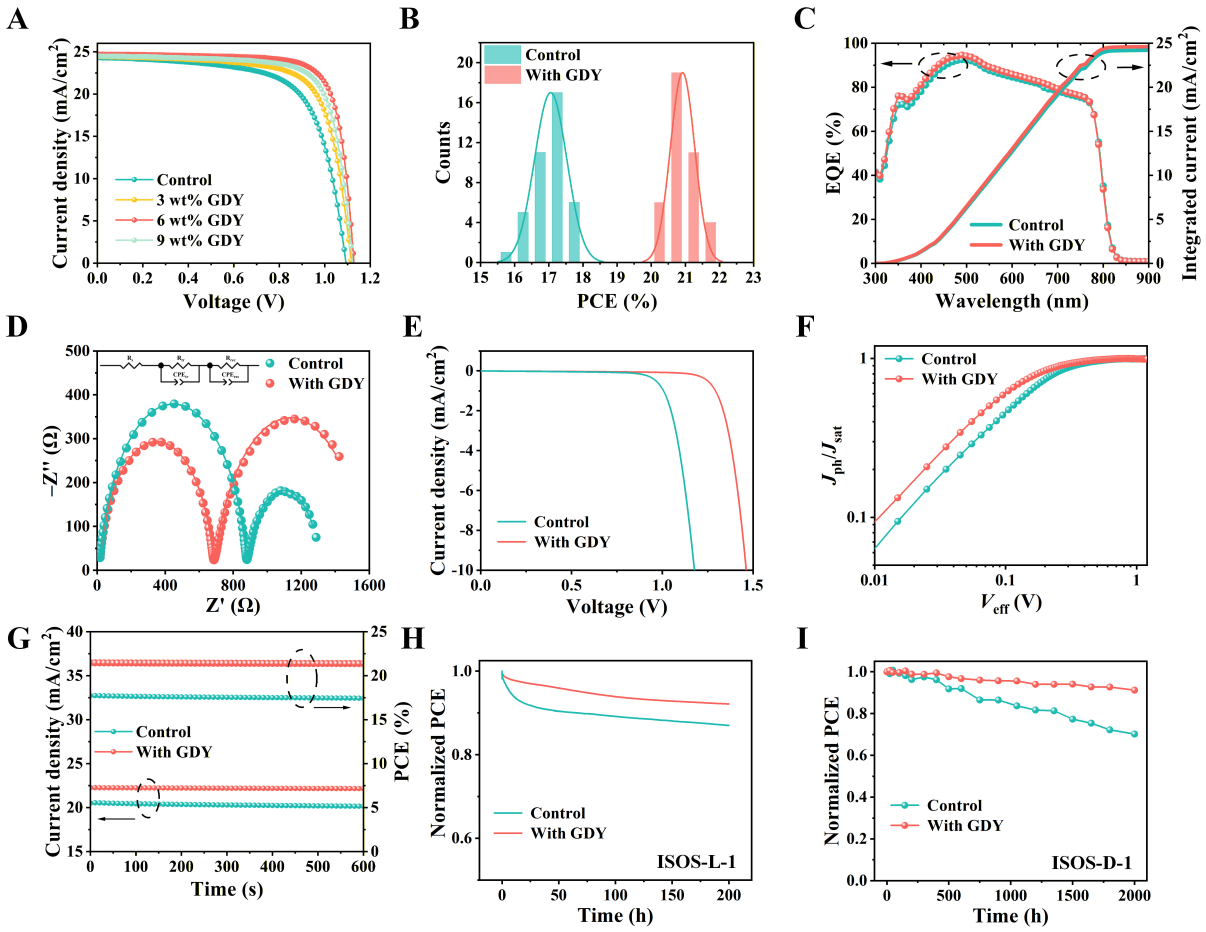


**Figure 5.** (A) *J-V* curves for PSCs containing different GDY loadings under one-sun illumination; (B) PCE statistical distribution of control and optimized GDY-modified PSCs; (C) EQE and integrated $J_{SC}$ curves; (D) Nyquist plots measured in the dark at a bias of 0.8 V, with the equivalent circuit model shown in the inset; (E) *J-V* curves under dark conditions; (F) Photocurrent density ($J_{ph}$) as a function of effective voltage ($V_{eff}$); (G) Stabilized current density and PCE under maximum-power-point tracking at one-sun illumination; (H) Operational stability under continuous illumination at the maximum-power point under the ISOS-L-1 protocol; (I) Long-term storage stability (ISOS-D-1) of unencapsulated devices in ambient air (30%-40% relative humidity) under dark conditions. Perovskite solar cells; GDY: graphdiyne; EQE: external quantum efficiency; *J-V*: current density-voltage; $J_{SC}$: short-circuit current density; ISOS-L-1: International Summit on Organic Photovoltaic Stability light-soaking protocol (level 1); ISOS-D-1: International Summit on Organic Photovoltaic Stability dark-storage protocol (level 1); $R_s$: series resistance; $R_{tr}$: transport resistance; $R_{rec}$: recombination resistance; $CPE_{tr}$: constant phase element associated with charge transport; $CPE_{rec}$: constant phase element associated with charge recombination; PCE: power conversion efficiency.

($V_{eff}$), with the quantities defined as follows[59]:

$$J_{ph} = J_L - J_D \tag{6}$$

$$V_{eff} = V_0 - V_{app} \tag{7}$$

where $J_L$ and $J_D$ refer to current densities recorded under one-sun illumination and in the dark; $V_0$ is the voltage at which $J_{ph}$ becomes zero, and $V_{app}$ is the externally applied voltage. As shown in Figure 5E and F, $J_{ph}$ approaches saturation more rapidly for the GDY-modified device. At the maximum-power point, the $J_{ph}/J_{sat}$ ratio increases from 0.842 for the control to 0.869 after GDY incorporation, indicating a higher charge-collection probability. This electrical response is consistent with the preferential carrier-transport function expected from the electronically coupled GDY/perovskite/carbon interface.

The stability of unencapsulated PSCs was subsequently evaluated. During maximum-power-point tracking (MPPT) under one-sun conditions [Figure 5G], the reference exhibits a stabilized current density of 20.15 mA $cm^{-2}$ and a PCE of 17.43%, compared with 22.16 mA $cm^{-2}$ and 21.38% for the GDY-containing device. In operational testing under continuous white-LED illumination at the maximum-power point (ISOS-L-1), 92% of the initial PCE remains after 200 h for the GDY-modified cell, versus 87% for the control [Figure 5H]. Dark storage in ambient air at 30%-40% relative humidity (ISOS-D-1) leads to retention of 91% and 70%, respectively, after 2,000 h [Figure 5I]. Both protocols therefore show improved stability following the introduction of GDY into the carbon electrode.

## CONCLUSIONS

In summary, we establish a graphdiyne-enabled interfacial transport-sieving effect in carbon electrode-based perovskite solar cells, reconciling efficient charge extraction with effective Pb sequestration at the perovskite/carbon interface. The π-conjugated framework of GDY bridges the energy-level mismatch and provides an energetically favorable pathway for hole extraction, increasing SCLC-derived effective hole mobility by approximately ninefold. Meanwhile, its electron-rich π system passivates undercoordinated $Pb^{2+}$ defects through π-electron coupling and interfacial charge redistribution, thereby reducing trap-state density and suppressing nonradiative recombination. Beyond these carrier-transport functions, the uniformly distributed sp-hybridized acetylenic linkages exhibit strong chemical affinity toward released Pb species, reducing lead leakage by up to 80%. Experimental analyses implicate the acetylenic motifs in Pb binding, while DFT calculations identify the corner configuration of the acetylenic ring as the energetically preferred adsorption geometry. Benefiting from this transport-selective interface, the optimized device achieves a champion PCE of 21.71% together with enhanced operational and storage stability. Further direct characterization of the contact interface will provide deeper mechanistic insight into the electronic selectivity. These findings establish interfacial transport sieving as a promising design principle for selectively facilitating desirable carrier transport while retaining hazardous Pb species, offering a new avenue toward efficient and environmentally responsible perovskite photovoltaics.

## DECLARATIONS

### Acknowledgments

The authors sincerely acknowledge Prof. Jiangjian Shi and Prof. Qingbo Meng of the Institute of Physics, Chinese Academy of Sciences for their assistance with transient photocurrent and transient photovoltage characterizations.

### Authors' contributions

Conceptualization: Sun, H.; Kang, Z.; Zhang, Y.
Methodology, writing - original draft: Sun, H.; Fan, W.; Xu, C.
Investigation: Sun, H.; Liu, Y.; Yu, L.
Formal analysis: Xu, C.; Wang, H.; Hu, L.
Data curation: Wang, H.; Hu, L.; Lu, Y.
Software: Xu, C.; Liu, Y.
Validation: Fan, W.; Yu, L.; Lu, Y.
Writing - review & editing, resources, supervision, funding acquisition: Liang, Z.; Kang, Z.; Zhang, Y.

### Availability of data and materials

The data supporting the findings of this study are available within this Article and its Supplementary Materials. Further data are available from the corresponding authors upon request.

### AI and AI-assisted tools statement

Not applicable.

### Financial support and sponsorship

This work was supported by the National Key Research and Development Program of China (No. 2021YFA1201800), National Natural Science Foundation of China (Nos. 52188101, 52122208, and 52402217), Scientific Research Innovation Capability Support Project for Young Faculty (No. FRF-U40-25-001), Fundamental and Interdisciplinary Disciplines Breakthrough Plan of the Ministry of Education of China (No. JYB2025XDXM411), National Key Research and Development Program of China (Nos. 2018YFA0703503, 2022YFA1204502, and 2023YFF1500402), State Key Laboratory for Advanced Metals and Materials (Nos. 2022Z-08 and 2023-Z13), Fundamental Research Funds for the Central Universities (Nos. GNYZ-2024-26, FRF-AT-25-007, GJJ2022-08, and FRF-TP-2021-03C1), and China Postdoctoral Science Foundation (Nos. GZB20240005 and 2024M750096).

## Conflicts of interest

All authors declare that there are no conflicts of interest.

## Ethical approval and consent to participate

Not applicable.

## Consent for publication

Not applicable.

## Copyright

© The Author(s) 2026.

## Supplementary Materials

Supplementary Materials

## REFERENCES

1. Wu, X.; Kou, W.; Li, Z.; et al. Electronic-resonance enhanced molecule for perovskite solar cells. *Nature* **2026**, *656*, 861-8. DOI
2. Harit, A. K.; He, Z.; Kuang, Y.; et al. Taking perovskite photovoltaics from promise to product. *Nat. Rev. Clean. Technol.* **2026**, *2*, 453-66. DOI
3. Li, B.; Gao, D.; Zhang, C.; et al. Closed-loop manufacturing for sustainable perovskite photovoltaics. *Nat. Rev. Mater.* **2026**, *11*, 10-25. DOI
4. Bach, U.; Lupo, D.; Comte, P.; et al. Solid-state dye-sensitized mesoporous $TiO_2$ solar cells with high photon-to-electron conversion efficiencies. *Nature* **1998**, *395*, 583-5. DOI
5. Shin, Y. S.; Lee, J.; Sung, M. J.; Jeon, I.; Jeon, N. J.; Kim, D. S. Intrinsic and extrinsic determinants of stability in Spiro-OMeTAD-based hole-transporting layers in perovskite solar cells: mechanistic insights and strategic perspectives. *Adv. Mater.* **2025**, *37*, e13270. DOI
6. You, S.; Zeng, H.; Liu, Y.; et al. Radical polymeric p-doping and grain modulation for stable, efficient perovskite solar modules. *Science* **2023**, *379*, 288-94. DOI
7. Liu, Y.; Zhang, Z.; Wu, T.; et al. Cost effectivities analysis of perovskite solar cells: will it outperform crystalline silicon ones? *Nano-Micro. Lett.* **2025**, *17*, 219. DOI PubMed PMC
8. Penukula, S.; Tippin, F.; Li, M.; Khawaja, K. A.; Yan, F.; Rolston, N. Use of carbon electrodes to reduce mobile ion concentration and improve reliability of metal halide perovskite photovoltaics. *Energy. Mater.* **2024**, *4*, 400060. DOI
9. Sajid, M.; Batool, H. S.; Su, Y.; Chen, F.; Lee, S. Recent advances in carbon-based materials for hole transport layer-free perovskite solar cells: a mini review. *Chin. Chem. Lett.* **2026**, 113323. DOI
10. Yu, B.; Shi, J.; Li, Y.; et al. Regulating three-layer full carbon electrodes to enhance the cell performance of $CsPbI_3$ perovskite solar cells. *Nat. Commun.* **2025**, *16*, 3328. DOI PubMed PMC
11. Zouhair, S.; Yoo, S.; Bogachuk, D.; et al. Employing 2D-perovskite as an electron blocking layer in highly efficient (18.5%) perovskite solar cells with printable low temperature carbon electrode. *Adv. Energy. Mater.* **2022**, *12*, 2200837. DOI
12. Zhang, C.; Liang, S.; Liu, W.; et al. $Ti_1$-graphene single-atom material for improved energy level alignment in perovskite solar cells. *Nat. Energy.* **2021**, *6*, 1154-63. DOI
13. Zhang, H.; Lee, J. W.; Nasti, G.; et al. Lead immobilization for environmentally sustainable perovskite solar cells. *Nature* **2023**, *617*, 687-95. DOI

14. Lin, D.; Huang, Y.; Chen, Q.; et al. Mitigating lead toxicity towards safer commercialization of perovskite solar cells. *Nat. Energy.* **2026**, *11*, 805-17. DOI
15. Cao, X.; Hu, T.; Qi, Y.; Niu, W.; Tang, B.; Zhang, S. Dual dynamic covalent bond adaptive networks for high-performance, HTL-free carbon-based perovskite solar cells. *Small* **2026**, *22*, e74903. DOI PubMed
16. Wang, W. T.; Holzhey, P.; Zhou, N.; et al. Water- and heat-activated dynamic passivation for perovskite photovoltaics. *Nature* **2024**, *632*, 294-300. DOI PubMed PMC
17. Yang, Y.; Chen, H.; Liu, C.; et al. Amidination of ligands for chemical and field-effect passivation stabilizes perovskite solar cells. *Science* **2024**, *386*, 898-902. DOI
18. Cai, Y.; Bai, Z.; Chen, C.; et al. Machine learning prediction of small molecule passivators and their impacts on the passivation and photocatalytic performance of organic-inorganic hybrid perovskite interfaces. *Energy. Mater.* **2025**, *5*, 500043. DOI
19. Xu, C.; Chen, X.; Ma, S.; et al. Interpretation of rubidium-based perovskite recipes toward electronic passivation and ion-diffusion mitigation. *Adv. Mater.* **2022**, *34*, e2109998. DOI
20. Zhou, S.; Fu, S.; Wang, C.; et al. Aspartate all-in-one doping strategy enables efficient all-perovskite tandems. *Nature* **2023**, *624*, 69-73. DOI
21. Wang, S.; Gong, X. Y.; Li, M. X.; Li, M. H.; Hu, J. S. Polymers for perovskite solar cells. *JACS. Au.* **2024**, *4*, 3400-12. DOI PubMed PMC
22. Chen, J.; Shao, C.; Wang, L.; et al. Conjugated polymer semiconductors enabled multifunctional interfacial engineering for high-performance inverted perovskite solar cells. *Adv. Mater.* **2026**, *38*, e73850. DOI
23. Li, Q.; Zheng, Y.; Wang, H.; et al. Graphene-polymer reinforcement of perovskite lattices for durable solar cells. *Science* **2025**, *387*, 1069-77. DOI
24. Agresti, A.; Pazniak, A.; Pescetelli, S.; et al. Titanium-carbide MXenes for work function and interface engineering in perovskite solar cells. *Nat. Mater.* **2019**, *18*, 1228-34. DOI
25. Zhao, P.; Shuang, Y.; Huo, J.; et al. Hybrid perovskite toughened by covalent organic framework fibers for mechanically reliable solar cells. *Trans. Mater. Res.* **2026**, *2*, 100398. DOI
26. Macdonald, T. J.; Clancy, A. J.; Xu, W.; et al. Phosphorene nanoribbon-augmented optoelectronics for enhanced hole extraction. *J. Am. Chem. Soc.* **2021**, *143*, 21549-59. DOI
27. Dai, K.; Wang, H.; Huang, W.; et al. Thermally independent interfacial reconstruction for phase-pure n = 1 2D perovskites with mixed-orientation surface architecture. *Adv. Mater.* **2026**, *38*, e74247. DOI
28. Li, X.; Zhang, F.; He, H.; Berry, J. J.; Zhu, K.; Xu, T. On-device lead sequestration for perovskite solar cells. *Nature* **2020**, *578*, 555-8. DOI
29. Zhuang, Q.; Xu, Z.; Li, H.; et al. Molecular polymerization strategy for stable perovskite solar cells with low lead leakage. *Sci. Adv.* **2025**, *11*, eado7318. DOI PubMed PMC
30. Ma, J.; Fan, S.; Shao, C.; et al. Double-chain copolymer network via in situ polymerization enables high-stability and lead-safe perovskite solar cells. *Angew. Chem. Int. Ed.* **2025**, *64*, e202425578. DOI
31. Chen, S.; Deng, Y.; Xiao, X.; Xu, S.; Rudd, P. N.; Huang, J. Preventing lead leakage with built-in resin layers for sustainable perovskite solar cells. *Nat. Sustain.* **2021**, *4*, 636-43. DOI
32. Li, G.; Li, Y.; Liu, H.; Guo, Y.; Li, Y.; Zhu, D. Architecture of graphdiyne nanoscale films. *Chem. Commun.* **2010**, *46*, 3256-8. DOI
33. Fang, Y.; Liu, Y.; Qi, L.; Xue, Y.; Li, Y. 2D graphdiyne: an emerging carbon material. *Chem. Soc. Rev.* **2022**, *51*, 2681-709. DOI
34. Kuang, J.; Yu, J.; Zhang, Q.; et al. Graphdiyne production in a flash: high-yield direct synthesis by electron beam irradiation. *Adv. Mater.* **2025**, *37*, e2506979. DOI
35. Zhang, X.; Chai, J.; Wang, C.; et al. Graphdiyne as a hole-transport channel in carbon nitride heterojunctions for synergistic $CO_2$ reduction and γ-butyrolactone synthesis. *Angew. Chem. Int. Ed.* **2026**, *65*, e3147768. DOI
36. Zhang, S.; Xu, C.; Fan, W.; et al. Sp-hybridized carbon enabled crystal lattice manipulation, pushing the limit of fill factor in β-$CsPbI_3$ perovskite solar cells. *Matter* **2024**, *7*, 3205-20. DOI
37. Liu, R.; Zhou, J.; Gao, X.; et al. Graphdiyne filter for decontaminating lead-ion-polluted water. *Adv. Elect. Mater.* **2017**, *3*, 1700122. DOI
38. Yuan, T.; Xiong, S.; Shen, X. Coordination of actinide single ions to deformed graphdiyne: strategy on essential separation processes in nuclear fuel cycle. *Angew. Chem. Int. Ed.* **2020**, *59*, 17719-25. DOI PubMed
39. Zhu, J.; Liu, D.; Li, C.; et al. Facile and large-scale synthesis of polymorphic graphdiyne catalyzed by transition metal salts for organic pollutant removal. *RSC. Adv.* **2021**, *11*, 35408-14. DOI PubMed PMC
40. Blöchl, P. E. Projector augmented-wave method. *Phys. Rev. B.* **1994**, *50*, 17953-79. DOI
41. Kresse, G.; Joubert, D. From ultrasoft pseudopotentials to the projector augmented-wave method. *Phys. Rev. B.* **1999**, *59*, 1758. DOI

42. Li, J.; Zhong, L.; Tong, L.; et al. Atomic Pd on graphdiyne/graphene heterostructure as efficient catalyst for aromatic nitroreduction. *Adv. Funct. Mater.* **2019**, *29*, 1905423. DOI
43. Wang, Z.; Zheng, Z.; Xue, Y.; He, F.; Li, Y. Acidic water oxidation on quantum dots of $IrO_x$/graphdiyne. *Adv. Energy. Mater.* **2021**, *11*, 2101138. DOI
44. Tan, Q.; Li, Z.; Luo, G.; et al. Inverted perovskite solar cells using dimethylacridine-based dopants. *Nature* **2023**, *620*, 545-51. DOI
45. Bu, T.; Li, J.; Li, H.; et al. Lead halide-templated crystallization of methylamine-free perovskite for efficient photovoltaic modules. *Science* **2021**, *372*, 1327-32. DOI
46. Wang, W.; Chen, P.; Chiang, C.; Guo, T.; Wu, C.; Feng, S. Synergistic reinforcement of built-in electric fields for highly efficient and stable perovskite photovoltaics. *Adv. Funct. Mater.* **2020**, *30*, 1909755. DOI
47. Wang, Z.; Han, Y.; Lin, X.; Cai, J.; Wu, S.; Li, J. An ensemble learning platform for the large-scale exploration of new double perovskites. *ACS. Appl. Mater. Interfaces.* **2022**, *14*, 717-25. DOI
48. Li, Y.; An, D.; Zhu, B.; Huang, Y.; Tang, G. Carrier mobility trends in nitride perovskites: first-principles insights and phenomenological models. *Phys. Rev. B.* **2026**, 114. DOI
49. Clarke, T. M.; Durrant, J. R. Charge photogeneration in organic solar cells. *Chem. Rev.* **2010**, *110*, 6736-67. DOI PubMed
50. Yang, G.; Wang, C.; Lei, H.; et al. Interface engineering in planar perovskite solar cells: energy level alignment, perovskite morphology control and high performance achievement. *J. Mater. Chem. A.* **2017**, *5*, 1658-66. DOI
51. Li, M.; Liu, S.; Qiu, F.; Zhang, Z.; Xue, D.; Hu, J. High-efficiency $CsPbI_2Br$ perovskite solar cells with dopant-free poly(3-hexylthiophene) hole transporting layers. *Adv. Energy. Mater.* **2020**, *10*, 2000501. DOI
52. Bai, C.; Shu, H.; Zhang, S.; Zhang, W.; Xu, Y.; Yang, S. Synergistic bulk and interface engineering of $SnO_2$ via ammonium formate for efficient and stable perovskite solar cells. *Trans. Mater. Res.* **2026**, *2*, 100335. DOI
53. Duan, L.; Liang, H.; Wu, L.; et al. Suppressing alkyl ammonium deprotonation with low-pKa solvent for reproduceable and stable high-efficiency perovskite solar cells. *Angew. Chem. Int. Ed.* **2026**, *65*, e10623. DOI
54. Glowienka, D.; Galagan, Y. Light intensity analysis of photovoltaic parameters for perovskite solar cells. *Adv. Mater.* **2022**, *34*, e2105920. DOI PubMed PMC
55. Shi, J.; Li, Y.; Li, Y.; et al. From ultrafast to ultraslow: charge-carrier dynamics of perovskite solar cells. *Joule* **2018**, *2*, 879-901. DOI
56. Jin, H.; Debroye, E.; Keshavarz, M.; et al. It's a trap! On the nature of localised states and charge trapping in lead halide perovskites. *Mater. Horiz.* **2020**, *7*, 397-410. DOI
57. Liang, Y.; Song, P.; Tian, H.; et al. Lead leakage preventable fullerene-porphyrin dyad for efficient and stable perovskite solar cells. *Adv. Funct. Mater.* **2022**, *32*, 2110139. DOI
58. Wang, N.; Li, X.; Tu, Z.; et al. Synthesis and electronic structure of boron-graphdiyne with an sp-hybridized carbon skeleton and its application in sodium storage. *Angew. Chem. Int. Ed.* **2018**, *57*, 3968-73. DOI
59. Dai, X.; Fan, B.; Zhou, W.; Xu, X.; Peng, Q. Mechanistic iron(III) doping of solution-processed $MoO_x$ enables universal, stable, and efficient hole transport in organic and perovskite solar cells. *Joule* **2026**, *10*, 102299. DOI


**Disclaimer/Publisher's Note:** All statements, opinions, and data contained in this publication are solely those of the individual author(s) and contributor(s) and do not necessarily reflect those of OAE and/or the editor(s). OAE and/or the editor(s) disclaim any responsibility for harm to persons or property resulting from the use of any ideas, methods, instructions, or products mentioned in the content.

© The Author(s) 2026. Open Access This article is licensed under a Creative Commons Attribution 4.0 International License (https://creativecommons.org/licenses/by/4.0/), which permits unrestricted use, sharing, adaptation, distribution and reproduction in any medium or format, for any purpose, even commercially, as long as you give appropriate credit to the original author(s) and the source, provide a link to the Creative Commons license, and indicate if changes were made.